



Stochastic and Quasi-adiabatic Electron Heating in Quasi-parallel Shocks

Krzysztof Stasiewicz^{1,2} and Bengt Eliasson³¹Department of Physics and Astronomy, University of Zielona Góra, Zielona Góra, Poland; krzy.stasiewicz@gmail.com²Space Research Centre, Polish Academy of Sciences, Warsaw, Poland³SUPA, Department of Physics, University of Strathclyde, Glasgow G4 0NG, UK; bengt.eliasson@strath.ac.uk

Received 2020 August 27; revised 2020 October 7; accepted 2020 October 8; published 2020 December 2

Abstract

Using Magnetospheric Multiscale observations at the Earth's quasi-parallel bow shock we demonstrate that electrons are heated by two different mechanisms: a quasi-adiabatic heating process during magnetic field compression, characterized by the isotropic temperature relation $T/B = (T_0/B_0)(B_0/B)^\alpha$ with $\alpha = 2/3$ when the electron heating function $|\chi_e| < 1$, and a stochastic heating process when $|\chi_e| > 1$. Both processes are controlled by the value of the stochastic heating function $\chi_j = m_j q_j^{-1} B^{-2} \text{div}(\mathbf{E}_\perp)$ for particles with mass m_j and charge q_j in the electric and magnetic fields \mathbf{E} and \mathbf{B} . Test-particle simulations are used to show that the stochastic electron heating and acceleration in the studied shock are accomplished by waves at frequencies $(0.4\text{--}5) f_{ce}$ (electron gyrofrequency) for bulk heating, and waves $f > 5 f_{ce}$ for acceleration of the tail of the distribution function. Stochastic heating can give rise to flat-top electron distribution functions, frequently observed near shocks. It is also shown that obliquely polarized electric fields of electron cyclotron drift and ion acoustic instabilities scatter the electrons into the parallel direction and keep the isotropy of the electron distribution. The results reported in this paper may be relevant to electron heating and acceleration at interplanetary shocks and other astrophysical shocks.

Unified Astronomy Thesaurus concepts: Planetary bow shocks (1246); Shocks (2086); Plasma astrophysics (1261)

1. Introduction

The observational advances enabled by multipoint measurements in space like Cluster (Escoubet et al. 1997), THEMIS (Sibeck & Angelopoulos 2008), and Magnetospheric Multiscale (MMS) (Burch et al. 2016) have stimulated significant progress in space plasma physics. Specifically, the recent MMS mission comprising four spacecraft flying through the bow shock and the magnetosheath in formation with separation distances of about 20 km has opened unprecedented possibility for testing theoretical models for heating and acceleration mechanisms that operate at collisionless shocks by detailed comparison with observations. Using these state-of-the-art measurements, which will also be discussed in Section 2 of the present paper, Stasiewicz (2020a, 2020b) and Stasiewicz & Eliasson (2020) have identified a chain of collective plasma processes that operate at both quasi-parallel and quasi-perpendicular bow shocks and lead to the heating of ions and electrons. This sequence involves cross-field current-driven instabilities and can be summarized as follows:

Shock compression of the number density N and magnetic field $B \rightarrow$ diamagnetic current \rightarrow lower hybrid drift (LHD) instability \rightarrow electron $\mathbf{E} \times \mathbf{B}$ drift \rightarrow modified two-stream (MTS) instability \rightarrow electron cyclotron drift (ECD) instability \rightarrow heating: quasi-adiabatic ($\chi_j < 1$), stochastic ($\chi_j > 1$).

The above chain of physical processes is triggered by a single event, namely, the compression of N and B characteristic for fast magnetosonic waves, so the above sequence could be present in all types of collisionless shock waves in space that are associated with density and magnetic field compression.

The stochastic heating function of particle species j ($j = e$ for electrons and p for protons) is (Stasiewicz 2020a, 2020b)

$$\chi_j(t, \mathbf{r}) = \frac{m_j}{q_j B^2} \text{div}(\mathbf{E}_\perp), \quad (1)$$

which is a generalization of the heating condition from earlier works of Karney (1979), McChesney et al. (1987), and Balikhin et al. (1993), where the divergence is reduced to the directional gradient $\partial E_x / \partial x$. The particles are magnetized (adiabatic) for $|\chi_j| < 1$, and demagnetized (subject to non-adiabatic heating) for $|\chi_j| \gtrsim 1$.

The high-quality electric field measurements by the FIELDS instrumentation suite on MMS (Ergun et al. 2016; Lindqvist et al. 2016; Torbert et al. 2016) makes it possible to directly calculate the divergence of the electric field that is used in Equation (1). The first time–frequency spectrogram of an approximation to $\text{div}(\mathbf{E}) = \rho / \epsilon_0$, i.e., of the electric charge distribution across the bow shock was published by Stasiewicz (2020a).

The proton heating function χ_p typically has values in the range 10–100 in the bow shock and the magnetosheath, which implies that the ions are strongly demagnetized and can be subject to stochastic heating processes in these regions.

At quasi-perpendicular shocks the derived values of χ_e for electrons are mostly below the stochastic threshold, due to the increasing values of $B \approx 10\text{--}40$ nT in the shock ramp combined with the scaling $\chi_e \propto B^{-2}$. Stasiewicz & Eliasson (2020) have shown that such situations instead lead to *quasi-adiabatic electron heating*, characterized by electron heating during the compression of the magnetic field while keeping the magnetic moment conserved. The perpendicular energy gain is redistributed to the parallel energy component by scattering on waves, leading to the isotropic temperature relation (Stasiewicz

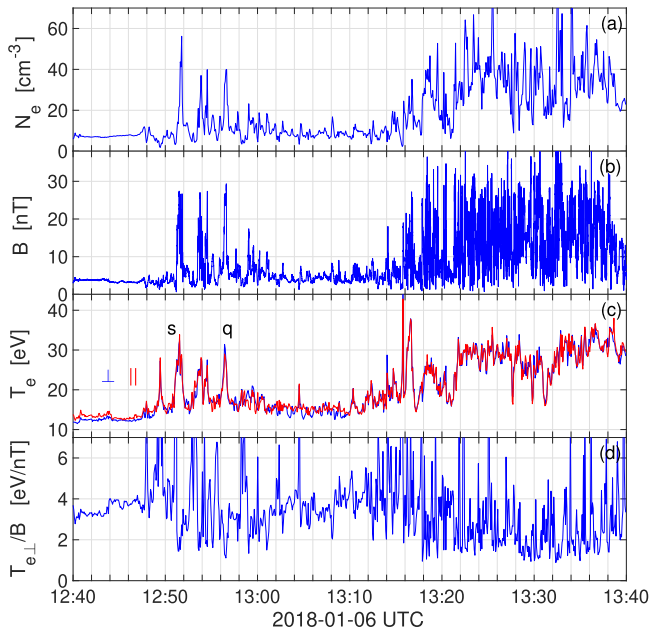


Figure 1. MMS-1 measurements from a 1 hr time interval of a quasi-parallel bow shock: (a) electron number density N_e and (b) magnetic field B form large-amplitude compressional structures (shocklets)—typical for parallel shocks. (c) Perpendicular and parallel temperatures of electrons, and (d) the ratio $T_{e\perp}/B$ that helps to identify the heating processes.

& Eliasson 2020)

$$\frac{T}{B} = \frac{T_0}{B_0} \left(\frac{B_0}{B} \right)^\alpha \quad (2)$$

with $\alpha = 1/3$, which predicts a dip of T/B where B has a maximum.

The aim of this paper is to make a detailed analysis of electron heating at quasi-parallel shocks, which complements the work of Stasiewicz & Eliasson (2020), concerned with ion and electron heating at quasi-perpendicular shocks.

2. Electron Heating in Quasi-parallel Shocks

We analyze MMS measurements from 2018 January 6 obtained by the three-axis electric field sensors (Ergun et al. 2016; Lindqvist et al. 2016; Torbert et al. 2016) and magnetic field vectors measured by the Fluxgate Magnetometer (Russell et al. 2016), and the number density, velocity, and temperature of both ions and electrons from the Fast Plasma Investigation (FPI) (Pollock et al. 2016).

When the interplanetary magnetic field is directed quasi-parallel to the shock normal, there is usually not a single ramp such as at the perpendicular bow shock, but instead an extended foreshock region is formed, filled with nonlinear compressional structures (shocklets) like the ones shown in Figures 1(a) and (b). These shocklets have spatial scales of ~ 1000 km and represent compressions of the plasma density and the magnetic field by a factor 2–10 times the background values (Schwartz & Burgess 1991; Stasiewicz et al. 2003; Lucek et al. 2008; Wilson et al. 2013). The large-amplitude shocklets are typically standing against the solar wind flow and move with speeds of the order tens of km s^{-1} with respect to the spacecraft. A frequently used awkward acronym for these structures is short large-amplitude magnetic structures (SLAMS), while the term “shocklets” is sometimes misleadingly used for long-wavelength $\sim R_E$, compressional magnetosonic waves.

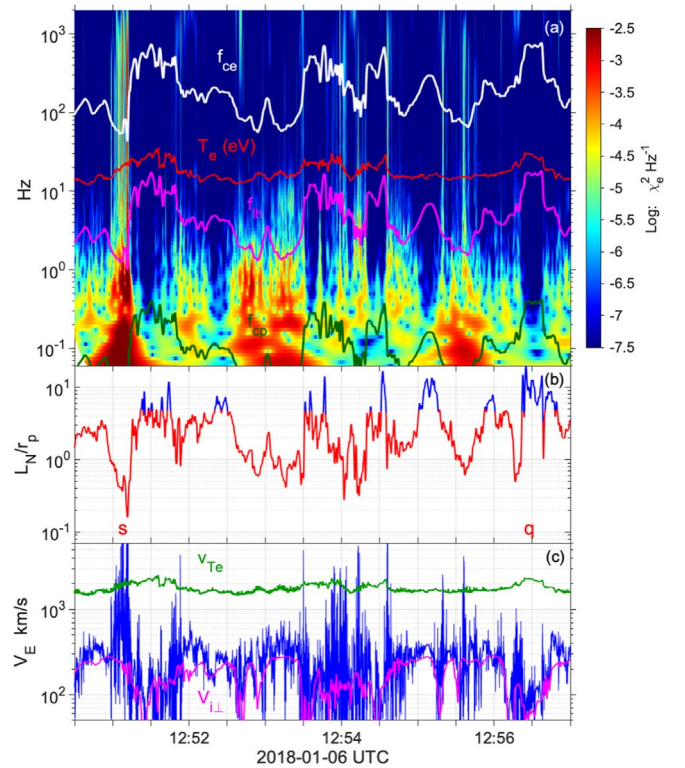


Figure 2. (a) Time vs. frequency spectrogram of χ_e for the time interval 12:50:30–12:57:00 UTC of Figure 1. Overplotted are the proton cyclotron frequency f_{cp} , the lower hybrid frequency f_{lh} , the electron cyclotron frequency f_{ce} , and the electron temperature $T_{e\perp}$ (eV, numerical values for the left scale apply). (b) The gradient scale of the plasma density L_N normalized with thermal proton gyroradius r_p (median = 200 km). Regions with $L_N/r_p \lesssim 5$ are unstable for the LHD instability (marked red). Markers for events “s” and “q” of Figure 1 are shown at the bottom. (c) The computed $\mathbf{E} \times \mathbf{B}$ drift speed V_E (blue), the electron thermal speed v_{Te} (green), and the ion perpendicular speed V_{\perp} (magenta). Waves between f_{cp} and f_{lh} are attributed to the LHD and above f_{lh} to the MTS instabilities, and for frequencies around f_{ce} and above to the ECD instability. Note the vertical striations that start from below 1 Hz (LHD instability) and go through the MTS and ECD instabilities up to 2 kHz, indicating co-location and common origin of these instabilities.

The large-amplitude compressions of N and B seen in Figures 1(a) and (b) are likely to trigger the chain of cross-field current-driven instabilities that can lead to the heating and acceleration of ions and electrons, as mentioned in Section 1. Indeed, in Figure 1(c) we see localized enhancements of the electron temperature, related to compressions of N and B , with almost equal perpendicular and parallel temperatures, $T_{e\perp} \approx T_{e\parallel}$. The ratio $T_{e\perp}/B$ shown in Figure 1(d) has been found to be a good indicator of the heating processes (Stasiewicz & Eliasson 2020). A flat ratio would indicate adiabatic process related to the conservation of the magnetic moment, but this is generally not observed. A dip in the ratio is characteristic to quasi-adiabatic processes described by Equation (2). A hump in the ratio may indicate nonadiabatic (possibly stochastic) heating, but may also be caused by other reasons, for example, as a magnetic depression not associated with heating, or a passage of a plasma cloud heated at an earlier time. Visible in Figure 1(d) are many humps and smaller-amplitude dips of $T_{e\perp}/B$, which indicate that both stochastic and quasi-adiabatic heating may be operational. The event marked “s” in Figure 1(c) is a representative for stochastic heating, and the event “q” for quasi-adiabatic heating. In these two events the electron temperature is increased by $\sim 100\%$, but there are

many smaller heating events, with a few percent increase of the electron temperature throughout the whole time interval.

In Figure 2 we make a detailed analysis of data for the time interval 12:50:30 to 12:57:00 UTC, which includes the “s” and “q” events. The median values for the plasma parameters during this time interval are the plasma beta $\beta_e \sim 2$, $\beta_i \sim 18$, the sound Mach number 1.5, the Alfvén Mach number 7, the electron gyrofrequency $f_{ce} \approx 154$ Hz, the thermal proton and electron gyroradii $r_p \approx 200$ km and $r_e \approx 2$ km, respectively, the perpendicular ion flow velocity $V_{i\perp} \approx 200$ km s⁻¹, and the electron and ion temperatures 20 and 120 eV, respectively. The position of these observations was (12.7, 6.9, 4.7) R_E GSE, and the average interspacecraft distance was 25 km.

In Figure 2(a) we show a time versus frequency spectrogram of χ_e with $\text{div}(\mathbf{E}_\perp)$ computed from four-point measurements using the method of Harvey (1998) developed for Cluster. Overplotted are the proton cyclotron frequency $f_{cp} = (eB/m_p)/2\pi$, the lower hybrid frequency $f_{lh} = (f_{cp}f_{ce})^{1/2}$, the electron cyclotron frequency $f_{ce} = (eB/m_e)/2\pi$, and the electron temperature $T_{e\perp}$ (eV).

There are concerns (Goodrich et al. 2018) that the axial double probe (ADP) on MMS, which uses rigid axial booms shorter than the wire booms of the spin-plane double probe experiment (SDP), produces larger-amplitude responses for short, tens of meter (Debye length) waves like ion acoustic (IA) waves. This instrumental asymmetry may be propagated and affect the computations of gradients of the electric field and the corresponding value of χ_e . For this reason, the computations of $\text{div}(\mathbf{E})$ are made in the despun spacecraft coordinates (DSL), which separate E_z provided by the ADP from (E_x, E_y) provided by the SDP. In these coordinates it is possible to remove the highest-frequency components above f_{ce} from the analysis, which may contain such short waves around the proton plasma frequency f_{pp} , or to not use the E_z component at all. For the purpose of the spectrogram shown in Figure 2(a) we applied rescaling of the E_z component to assure that $\text{rms}(E_z) = \text{rms}(E_y)$.

Figure 2(b) shows the gradient scale length $L_N = N/|\nabla N|^{-1}$ for the electron density N derived from data using the method of Harvey (1998). When the scale of the density gradient obeys the condition $L_N/r_p < (m_p/m_e)^{1/4}$ the ion diamagnetic drift $V_{di} = T_p(m_p\omega_{cp}L_N)^{-1} = v_{TP}(r_p/L_N)$ exceeds the threshold for the onset of the LHD instability (Davidson et al. 1977; Drake et al. 1983; Gary 1993). Here, $v_{TP} = (T_{p\perp}/m_p)^{1/2}$ is the proton thermal speed and $r_p = v_{TP}/\omega_{cp}$ the proton Larmor radius.

Waves between f_{cp} and f_{lh} in panel (a) are related to the LHD instability, which has maximum growth rate at $k_\perp r_e \sim 1$ (Davidson et al. 1977); however, simulation results of Daughton (2003) indicate that they have longer wavelengths $k_\perp(r_e r_p)^{1/2} \sim 1$ and electromagnetic character with significant magnetic fluctuations, which are observed also in the present case. Here, k_\perp is the wavenumber perpendicular to the magnetic field, and $r_e = v_{Te}/\omega_{ce}$ is the electron thermal Larmor radius, and $v_{Te} = (T_{e\perp}/m_e)^{1/2}$ is the electron thermal speed.

The enhanced electric field of the LHD waves produces strong $\mathbf{E} \times \mathbf{B}$ drifts of electrons only, because the ions are not subject to this drift due to their large gyroradius in comparison to the width of drift channels. When the electron-ion drift exceeds the ion thermal velocity, the MTS instability can also be excited, which may be responsible for the waves observed with frequencies above f_{lh} (Lashmore-Davies & Martin 1973; Gary et al. 1987; Umeda et al. 2014). The MTS and LHD instabilities belong to the same dispersion surface (Silveira et al. 2002; Yoon & Lui 2004), so we will not make a

distinction between these instabilities and use the term LHD instability in the sense of a generalized cross-field current-driven instability in the lower hybrid frequency range.

When the relative electron-ion drift speed becomes a significant fraction of the electron thermal speed, $V_E = |\mathbf{E} \times \mathbf{B}|/B^2 \sim v_{Te}$, the ECD instability is initiated, which creates even larger electric fields on spatial scales of r_e and smaller (Lashmore-Davies 1971; Forslund et al. 1972; Muschietti & Lembége 2013; Janhunen et al. 2018).

This process can be inferred from Figure 2(c), which shows the electric drift speed V_E computed from the measured electric field in the frequency range 0–256 Hz (blue curve). The highest frequencies were removed because at $f > f_{ce}$ the electron drift approximation is not valid. For comparison we also plot the electron thermal speed v_{Te} and the measured perpendicular speed of the ions $V_{i\perp}$ (magenta). Large values of $V_E \sim v_{Te}$ are signatures of large electric fields ($E \sim 100$ mV m⁻¹) of ECD waves that may be Doppler downshifted and observed also below f_{ce} . Large differences between the electron drift V_E and the measured perpendicular drift of ions $V_{i\perp}$ would induce sequentially the MTS and ECD instabilities after initiation of the LHD instability on the density gradients. The high V_E drift regions in Figure 2(c) are manifestations of spatially coupled LHD, MTS, and ECD instabilities.

The ECD instability is driven by the cyclotron resonance $\omega - k_\perp V_{de} = n\omega_{ce}$, where n is an integer, and $V_{de} \approx V_E$ is the electron drift velocity in the rest frame of ions (Janhunen et al. 2018). For ω near cyclotron harmonics this resonance condition is $k_\perp V_E \approx n\omega_{ce}$, which can be expressed equivalently by

$$k_\perp r_e \approx \frac{nv_{Te}}{V_E}, \quad (3)$$

which implies that the wavelength is

$$\lambda \approx 12.6 \text{ (km)} \frac{V_E}{nv_{Te}}, \quad (4)$$

with the numerical coefficient given for $r_e = 2$ km. This means that ECD waves with $n = 1$ and electric drift velocities $V_E > v_{Te}$ have wavelengths that enable accurate gradient computations needed for the calculations of $\text{div}(\mathbf{E})$ by the MMS spacecraft constellation. Because of short wavelengths, the higher harmonics $n > 1$ may be Doppler downshifted by ~ 100 Hz and observed in the $f_{lh} - f_{ce}$ frequency range. Their contribution to χ_e will be underestimated by the gradient computation procedure.

It should be emphasized that derivatives $\partial E_x/\partial x$, $\partial E_y/\partial y$, $\partial E_z/\partial z$ needed for the $\text{div}(\mathbf{E})$ computation depend on the partial separations of the satellites and not on the radial distances. The partial separations can be much smaller than the radial ones. For example, in the analyzed case we have $\Delta x_{14} = 0.3$ km, $\Delta y_{34} = 4$ km, and $\Delta z_{13} = 0.8$ km. In the case of waves propagating in the x -direction, satellites “1”–“4” could accurately capture gradients on a 1 km scale, while satellites “1”–“3” would capture correctly a ~ 1 km wave propagating in the z -direction. This is under assumption that the transverse scale of the wave front is larger than the tetrahedron. For an arbitrary wave one should find similar values for projections of the relative vector $(\mathbf{r}_i - \mathbf{r}_j)$ on the wave propagation direction. Thus, the accuracy of the gradient determination by the Harvey (1998) method is generally better than the nominal radial distances between the satellites (~ 20 km) would imply.

Waves around f_{ce} and above that are associated with the ECD instability have been observed at the bow shock as discussed by

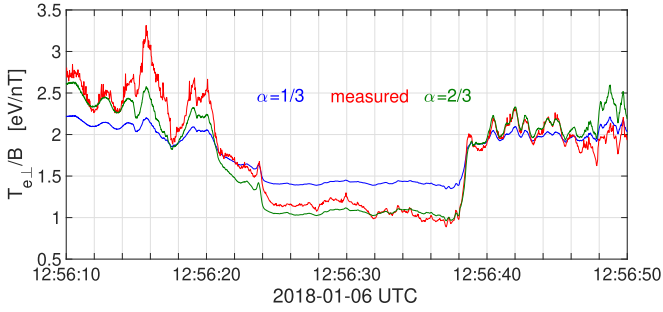


Figure 3. Comparison of the measured ratio $T_{e\perp}/B$ with Equation (2) for the event labeled “q” in Figure 2(d). The measured curve is in red, modeled for $\alpha = 1/3$ in blue, and modeled for $\alpha = 2/3$ in green. The latter gives a better fit with observations as further explained in the text.

Wilson et al. (2010), Breneman et al. (2013), Goodrich et al. (2018), and Stasiewicz (2020a). These waves have both a perpendicular component of the electric field and a comparable parallel E_{\parallel} component, related to IA waves (Fuselier & Gurnett 1984; Mozer & Sundqvist 2013; Goodrich et al. 2018).

2.1. Quasi-adiabatic Heating: Event “q”

The quasi-adiabatic event “q” in Figure 1(c) is clearly related to the compression of B shown in panel (b), and a dip in the $T_{e\perp}/B$ ratio shown in panel (d). Figure 3 shows a detailed comparison between the measured ratio in red color and the theoretical expression (2) with $\alpha = 1/3$ in blue. We also show the third curve in green, computed with $\alpha = 2/3$, which fits the observations significantly better than with $\alpha = 1/3$.

Equation (2) was derived by Stasiewicz & Eliasson (2020) with the following justification. When the magnetic moment is conserved, i.e., $T_{\perp}/B = \text{const}$, the differential temperature increase is $dT_{\perp} = T_{\perp} B^{-1} dB$. If the energy gain from 2 perpendicular degrees of freedom ($2dT_{\perp}$) is redistributed by pitch angle scattering to 3 degrees of freedom ($3dT$) the conservation of energy implies

$$3dT = 2TB^{-1}dB \quad (5)$$

for $T = T_{\perp} = T_{\parallel}$. The solution of this equation is given by (2) with $\alpha = 1/3$, and provides a very good approximation to the ratio measured in perpendicular shocks (Stasiewicz & Eliasson 2020). The fit is not as good in the present case. Let us make a reasonable assumption that there are additional sinks of energy, and an amount $\delta W = 3dT$ goes for the production of waves, in addition to $3dT$ for the isotropization. The modified energy equation is

$$6dT = 2TB^{-1}dB, \quad (6)$$

which has the solution (2) with exponent $\alpha = 2/3$.

A plausible explanation for the difference between the quasi-adiabatic response in quasi-perpendicular shocks ($\alpha = 1/3$) and in the present case of quasi-parallel shocks ($\alpha = 2/3$) is that in the previous case the waves engaged with the isotropization were generated by $\mathbf{E} \times \mathbf{B}$ electron drift caused by lower-frequency waves, so the whole energy gain from adiabatic perpendicular heating was used for isotropization. In the present case, the waves performing isotropization are fed by the adiabatic buildup of the temperature anisotropy. There are high-frequency electrostatic waves and whistlers ~ 100 Hz associated with this case, which may provide the required sink of kinetic energy. There may be other redistributions of the

energy in other cases, and the values of α may be found different from $\alpha = 1/3, 2/3$. The correspondence of the two curves in Figure 3 indicates outstanding quality of particle measurements by the FPI instrument (Pollock et al. 2016), which is able to reproduce the subtle effects of Equation (2) in sharp gradients of the shocklet in event “q.”

2.2. Observations of the Stochastic Heating

In Figure 2(a) waves between $f_{cp} - f_{lh}$ are attributed to the LHD and above f_{lh} to the MTS instabilities, and for frequencies around f_{ce} and above to the ECD instability. Note the vertical striations that start from below 1 Hz (LHD instability) and go through the MTS and ECD instabilities up to 2 kHz, indicating co-location and common origin of these instabilities. The profile of the magnetic field can be seen in plots of the plasma frequencies f_{cp}, f_{lh}, f_{ce} , which are all proportional to B , and directly in Figure 1(b). The stochastic heating event “s” occurs in a region with strong density gradients in panel (b), at the foot of a large-amplitude shocklet seen in the frequency plots. It is associated with $\chi_e \sim 10$ and a strong spectrum, which rapidly quenches just after 12:51:15 when the magnetic field increases. After this time the heating mostly continues as compressional, quasi-adiabatic with $|\chi_e| < 1$.

It is remarkable that the measured density gradient in panel (b) appears to obey the instability condition derived some 40 years ago (Davidson et al. 1977; Drake et al. 1983), $L_N/r_p < (m_p/m_e)^{1/4} \approx 6$, for the onset of the LHD instability. The LHD waves are seen in panel (a) below the lower hybrid frequency. The unstable regions are marked in red in panel (b).

The data presented in Figures 2(a)–(c) show correlations between the density gradients (panel (b)) and strong V_E drifts induced by large electric fields of LHD/ECD waves (panel (c)). The V_E values, determining the drift of electrons are much larger than the measured drift of ions $V_{i\perp}$, which would trigger consecutively the LHD/MTS and ECD instabilities that have different thresholds.

All of these signatures support the suggested heating scenario at shocks, which starts with the compression of N and B , then develops LHD/MTS/ECD instabilities on the gradients and induced drift velocities, and further lead to either quasi-adiabatic or stochastic heating controlled by the stochastic function χ_j (Stasiewicz 2020a, 2020b; Stasiewicz & Eliasson 2020).

Plasma structures with oppositely directed currents and turbulence characteristic for quasi-parallel shocks create minima of B , or even $B \sim 0$ regions (see Figure 1(b)), so that regions with $|\chi_e| > 1$ and associated stochastic heating are more common in parallel shocks than in perpendicular ones.

In this paper we focus on the electron heating, but it is worth mentioning that in the case of Figure 2 we observe spectacular stochastic heating of ions. Protons are rapidly heated from 40 to 500 eV with suprathermal tails accelerated to ~ 10 keV in three bursts related to the enhancements of the lower hybrid drift waves seen in panel (a). The stochastic ion bulk heating by LHD waves ($f_{cp} < f < f_{lh}$) and the tail acceleration mechanism by LH(MTS) waves ($f \gtrsim f_{lh}$) is universal, the same as in quasi-perpendicular shocks analyzed by Stasiewicz & Eliasson (2020).

To assess which wave frequencies and wavelengths from a broad spectrum of Figure 2 contribute most to the stochastic heating and isotropization of electrons we perform test-particle simulations described in the next section.

3. Simulations of Stochastic Heating and Isotropization

We follow the simulation setup described in detail by Stasiewicz & Eliasson (2020), extended here by including a magnetic-field-aligned component of the electrostatic wave field. The parallel component of the wave electric field is essential for isotropization processes. We consider a spacecraft/observer coordinate system in which the magnetic field B_0 is in the z -direction, and a macroscopic convection electric field $E_y = E_{0y}$ drives particles into an electrostatic wave with electric field $(E_x, E_z) = (E_{0x}, E_{0z})\cos(k_x x + k_z z - \omega_s t)$ with frequency ω_s in the spacecraft frame, propagating in the x - z plane, at angle θ to the magnetic field, where $\tan(\theta) = E_x/E_z = k_x/k_z$. We keep the magnetic field constant to separate purely stochastic heating from the quasi-adiabatic heating in compressed magnetic fields. Thus, in the Doppler-shifted frame of the satellite, the drifting plasma is characterized by the convecting electric field and the time-dependent wave electric field. The governing equations for particles with mass m and charge q are

$$m \frac{dv_x}{dt} = qE_{0x} \cos(k_x x + k_z z - \omega_s t) + qv_y B_0, \quad (7)$$

$$m \frac{dv_y}{dt} = qE_{0y} - qv_x B_0, \quad (8)$$

$$m \frac{dv_z}{dt} = qE_{0z} \cos(k_x x + k_z z - \omega_s t), \quad (9)$$

$$\frac{dx}{dt} = v_x, \quad \frac{dy}{dt} = v_y, \quad \frac{dz}{dt} = v_z. \quad (10)$$

By a change of frame into that of the $\mathbf{E} \times \mathbf{B}$ -drift velocity (the plasma frame),

$$v_x = V_x + \frac{E_{0y}}{B_0}, \quad x = X + \frac{E_{0y}}{B_0} t, \quad (11)$$

and the wave frequency in the plasma frame becomes $\omega = \omega_s - k_x E_{0y}/B_0$, incorporating the electric drift velocity. Using dimensionless variables with time normalized by ω_c^{-1} , space by k_x^{-1} and velocity by ω_c/k_x with $\omega_c = qB_0/m$ being the angular cyclotron frequency, gives the system of dimensionless, primed variables:

$$\frac{dv'_x}{dt'} = \chi \cos(x' + \kappa z' - \Omega t') + v'_y, \quad (12)$$

$$\frac{dv'_y}{dt'} = -v'_x, \quad (13)$$

$$\frac{dv'_z}{dt'} = \chi \kappa \cos(x' + \kappa z' - \Omega t'), \quad (14)$$

$$\frac{dx'}{dt'} = v'_x, \quad \frac{dy'}{dt'} = v'_y, \quad \frac{dz'}{dt'} = v'_z, \quad (15)$$

where $\kappa = k_z/k_x = E_{0z}/E_{0x} = 1/\tan(\theta)$ describes the direction of the electrostatic wave to the magnetic field,

$$\Omega = \omega_c^{-1}(\omega_s - k_x E_{0y}/B_0) \quad (16)$$

is the normalized wave frequency in the plasma frame, and

$$\chi = \frac{k_x E_{0x}}{\omega_c B_0} \quad (17)$$

is the stochastic heating parameter, equivalent to Equation (1), representing the normalized perpendicular component of the wave amplitude. The normalized parallel component of the wave amplitude $\chi \kappa$ in Equation (14) is found in Section 3.2 to be responsible for the isotropization of the distribution function. Stochastic motion takes place only in restricted regions in phase space (Fukuyama et al. 1977; Karney 1979; McChesney et al. 1987), and hence the initial velocity may also be considered a parameter. For a statistical description of the particles, the initial condition is taken to be a bi-Maxwellian distribution function, which in normalized variables takes the form

$$F' = \frac{1}{(2\pi)^{3/2} v'_{x0}{}^3 \tau^{1/2}} \exp\left(-\frac{(v'^2_x + v'^2_y + v'^2_z/\tau)}{2v'^2_{x0}}\right), \quad (18)$$

where $v'_{x0} = k_x r_c$ is the normalized thermal speed, $r_c = v_{T_{\perp 0}}/\omega_c$ is the thermal Larmor radius, and $\tau = T_{\parallel 0}/T_{\perp 0}$ is the initial parallel-to-perpendicular temperature ratio; we will use $\tau = 0.01$ below. Here $v_{T_{\perp 0}} = (T_{\perp 0}/m)^{1/2}$ is the initial thermal speed and $T_{\perp 0}$ is the initial perpendicular temperature. The value of v'_{x0} determines the initial temperature in the velocity distribution function, which, due to the normalization, is in fact proportional to the ratio of the gyroradius to the wavelength $\lambda = 2\pi/k_x$. The perpendicular kinetic temperature resulting from the stochastic heating is calculated as

$$T_{\perp} = m(\langle v'^2_z \rangle - \langle v'_x \rangle^2 + \langle v'_y \rangle^2 - \langle v'_y \rangle^2)/2, \quad (19)$$

while the parallel temperature is obtained as

$$T_{\parallel} = m(\langle v'^2_z \rangle - \langle v'_z \rangle^2), \quad (20)$$

and the total kinetic temperature $T = (2T_{\perp} + T_{\parallel})/3$. Here the angular brackets denote averages over particles, $\langle u \rangle = (\sum_{k=1}^M u_k)/M$. The system (12)–(15) is advanced in time using a Störmer–Verlet scheme (Press et al. 2007).

3.1. Simulations of the Perpendicular Heating

The above derived simulation equations will first be used to study the perpendicular heating in parameter space $(\Omega, k_x r_c, \chi)$, so we set $\theta = 90^\circ$. We carry out a set of test-particle simulations for $M = 10,000$ particles, which are Maxwell distributed in velocity and uniformly distributed in space. The input variables for the simulations are the normalized wave frequency Ω in the range 10^{-2} – 10^3 , and the initial normalized thermal velocity $v'_{x0} = k_x r_c$ spanning 10^{-2} – 10^3 . The normalized amplitude of the electrostatic wave is set to $\chi = 10$, consistent with the “s” event in Figure 2(d).

Simulations are carried out for different values of Ω and v'_{x0} to produce the color plot in Figure 4, which shows the difference $T'_{\perp} - T'_{\perp 0}$ between the normalized kinetic temperature $T'_{\perp} = k_x^2 T_{\perp}/m\omega_c^2$ at the end of the simulation and the initial value $T'_{\perp 0} = (v'_{x0})^2 = k_x^2 T_{\perp 0}/m\omega_c^2$.

The simulations are run for 30 cyclotron periods of the particles to primarily study electron heating, while in the previous case (Stasiewicz & Eliasson 2020) focused on ion heating, the time was three periods, and $\chi = 60$. However, the colormaps in Figure 4 and in the previous paper are applicable for any charged particle species. Comparing these two maps we see that the limiting upper frequency for the bulk heating is determined by the value of χ . In this case for $\chi = 10$ it is

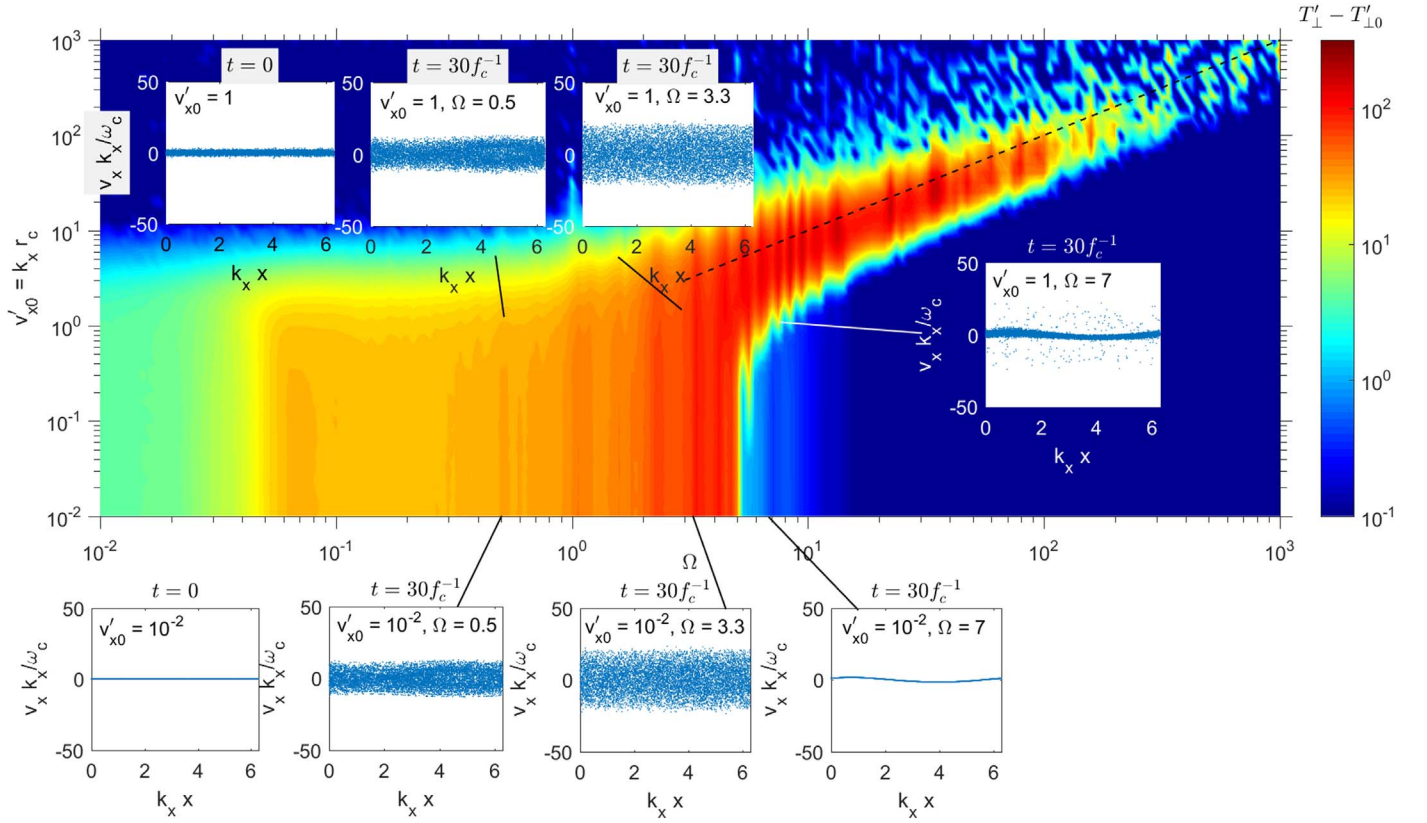


Figure 4. A color plot of stochastic heating showing the difference between the final and initial temperatures, $T'_\perp - T'_{\perp 0}$, after 30 cyclotron periods, for charged particles in an electrostatic wave with normalized electric field amplitude $\chi = 10$ directed perpendicularly to the magnetic field, $\theta = \pi/2$. Here $f_c = \omega_c/2\pi$, $T'_{\perp 0} = v'_{x0}{}^2$ is the normalized initial temperature and $v'_{x0} = k_x v_{T\perp 0}/\omega_c$ with the thermal speed $v_{T\perp 0} = (T_{\perp 0}/m)^{1/2}$. The insets show distribution functions in (x, v_x) space at $t = 0$ and $30f_c^{-1}$ for different values of Ω and v'_{x0} . Bulk heating takes place for $\Omega \lesssim 5$, while for $\Omega \gtrsim 5$ there is significant heating only for thermal velocity comparable to the phase velocity, or $v'_{x0} \sim \Omega$ in the normalized variables (dashed line) leading to a distribution function having a high-energy tail of particles.

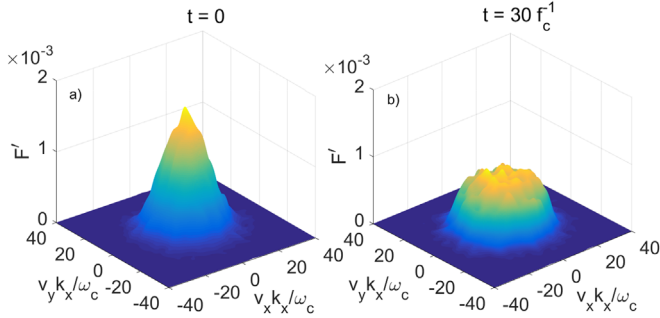


Figure 5. The formation of a flat-top electron distribution for $\chi = 10$, $\Omega = 3.3$, and $v'_{x0} = 10$. The initial Maxwell distribution (a) at $t = 0$ becomes the flat-top distribution (b) after $t = 30f_c^{-1}$.

$\Omega \approx 5$, while for $\chi = 60$ this boundary moves up to $\Omega \approx 10$. On the other hand, the lower frequency of the bulk heating region extends to lower values with increasing interaction time. It was at $\Omega \approx 1$ after 3 cyclotron periods for $\chi = 60$, and moved down to $\Omega \approx 0.05$ after 30 cyclotron periods in the present case.

Strong electron heating is seen for frequencies above f_{ce} , but a weak heating region extends down to lower hybrid frequencies $\Omega \sim 0.03$. Waves at lower frequencies have longer wavelengths and the electric field amplitude usually much smaller than the ECD waves, so they would produce typically

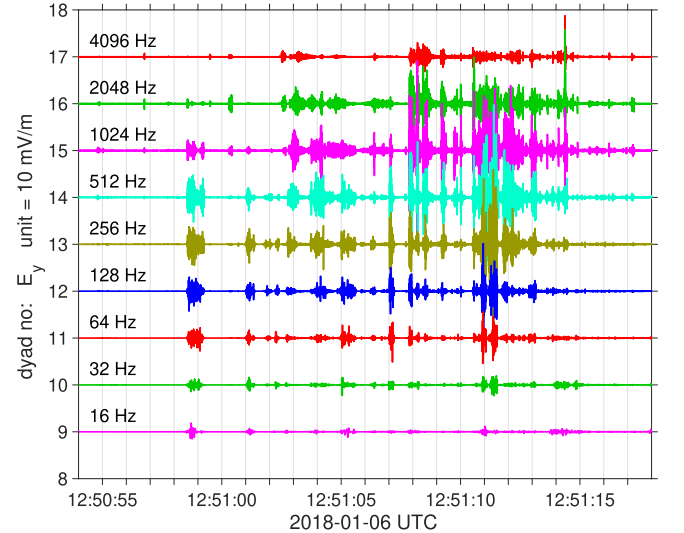


Figure 6. Decomposition of the measured electric signal E_y of waves during the stochastic event “s” into discrete frequency dyads using orthogonal wavelets. Unit amplitude is 10 mV m^{-1} .

$\chi_e < 1$. Thus, the $\sim f_{lh}$ frequency waves should not be capable to heat perpendicularly the electron population.

To visualize the effect of the stochastic mechanism on the particle distribution function we perform a test-particle simulation with $\chi = 10$, $\Omega = 3.3$, and $v'_{x0} = 10$ shown in

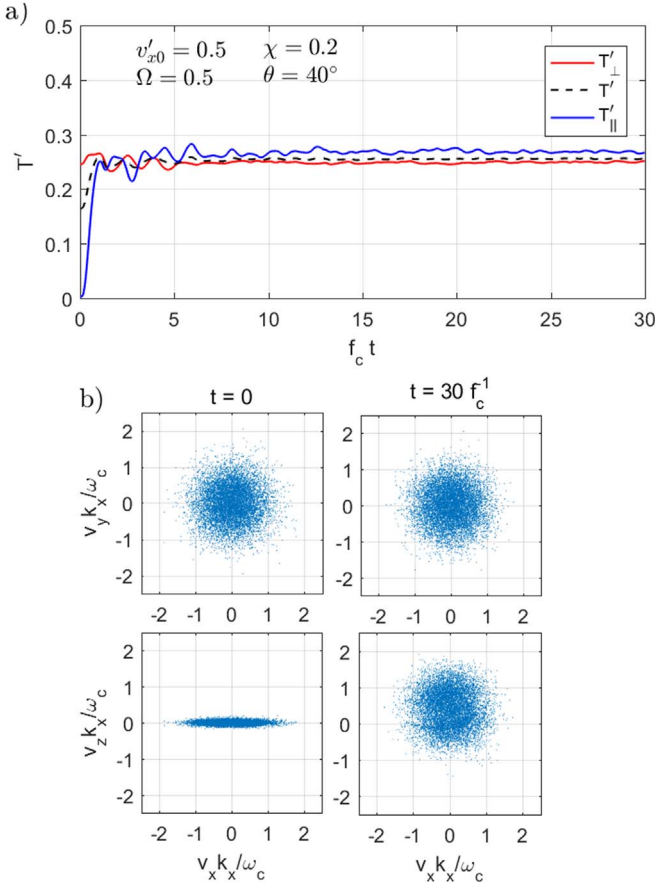


Figure 7. Isotropization of electrons showing (a) the time development of the kinetic temperatures, and (b) the distribution function at initial time $t = 0$ (left column) and final time $t = 30 f_c^{-1}$ (right column), projected in the v_x - v_y plane (top row) and in the v_x - v_z plane (bottom row), for $\theta = 40^\circ$, $\chi = 0.2$, $\Omega = 0.5$, and $v'_{x0} = 0.5$ with the initial temperature anisotropy $\tau = T_{\parallel 0}/T_{\perp 0} = 0.01$. The distribution function becomes isotropic within a few cyclotron periods.

Figure 5. We observe that the initially Maxwellian distribution function forms a flat-top distribution after 30 electron cyclotron periods. Flat-top electron distributions are commonly observed at shocks (Feldman et al. 1983; Lefebvre et al. 2007), and these observations can be explained by the stochastic mechanism discussed in this paper.

3.1.1. Stochastic Heating: Event “s”

Now we shall apply the simulation results to the case “s” of Figures 1(c) and 2, i.e., to the time interval 12:50:55 to 12:51:15 to identify waves responsible for the observed electron heating. During this time interval the mean values of plasma parameters are $v_{Te} = 2000 \text{ km s}^{-1}$, $r_e = 4 \text{ km}$, $r_p = 600 \text{ km}$, $f_{ce} = 80 \text{ Hz}$, $f_{lh} = 2 \text{ Hz}$, and $B = 3 \text{ nT}$. In Figure 6 we show the E_y component of the measured waves in the DSL coordinate system (close to GSE) decomposed into discrete frequency dyads with orthogonal wavelets (Mallat 1999). Orthogonality means that the time integral of the product of any pair of the frequency dyads is zero, and the decomposition is exact, i.e., the sum of all components gives the original signal.

We note first in Figure 6 that waves in channel 512 Hz have $\Omega = 6.4$, so this channel and all higher frequencies are beyond the parameter region of bulk heating of electrons. They can provide only acceleration for the tail of the distribution.

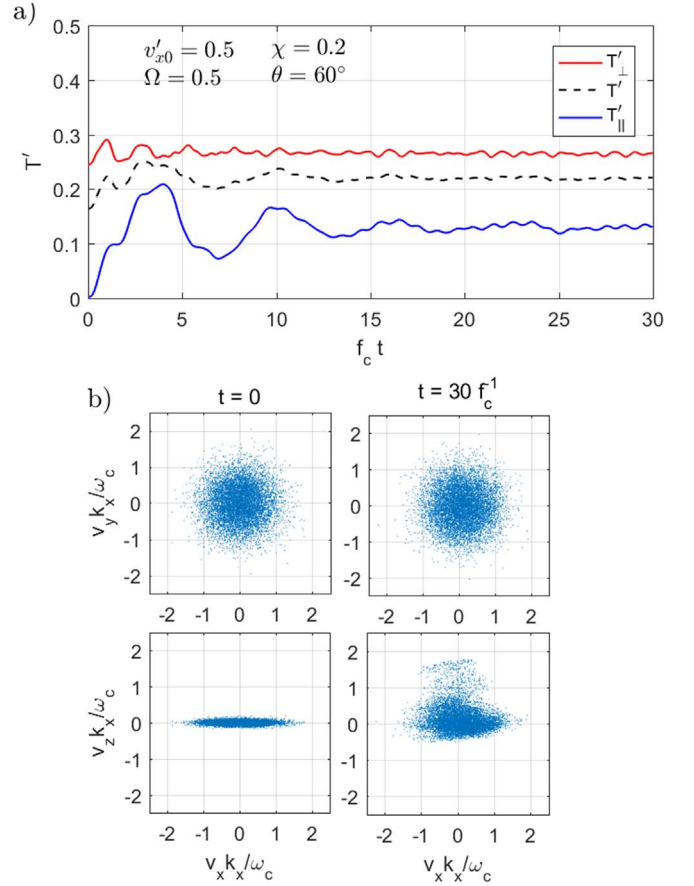


Figure 8. Isotropization of electrons showing (a) the time development of the kinetic temperatures, and (b) the distribution function at initial time $t = 0$ (left column) and final time $t = 30 f_c^{-1}$ (right column), projected in the v_x - v_y plane (top row) and in the v_x - v_z plane (bottom row), for $\theta = 60^\circ$, $\chi = 0.2$, $\Omega = 0.5$, and $v'_{x0} = 0.5$ with the initial temperature anisotropy $\tau = T_{\parallel 0}/T_{\perp 0} = 0.01$. The distribution function becomes only partially isotropic with a velocity tail of electrons along v_z .

Channels 32–256 Hz correspond to $(0.4\text{--}3.2) f_{ce}$ so they are most likely ECD waves responsible for the observed stochastic electron heating with the leading role of the channel 256 Hz ($\Omega = 3.2$) showing the largest amplitude, and providing the most efficient heating according to Figure 4.

The colormap shows that the bulk heating extends up to $K \equiv k_x r_e \approx 10$, which implies that the bulk heating of the thermal population has to be done by waves $0.4 f_{ce} \lesssim f < 5 f_{ce}$ with wavelengths longer than

$$\lambda_K = 2\pi r_e / K \approx 2.5 \text{ km}, \quad (21)$$

which means that the electrostatic waves or solitary structures on the Debye length scales would not participate in the perpendicular bulk heating of electrons. Lower hybrid waves, whistlers, and magnetosonic waves at $f \lesssim f_{lh}$ are also excluded.

An interesting question is why the ECD waves with a modest amplitude of 10 mV m^{-1} (Figure 6) produce $\chi_e \sim 10$ and stochastic heating in the present case, while waves at amplitude 100 mV m^{-1} give only $\chi_e < 1$ and quasi-adiabatic heating in perpendicular shocks (Stasiewicz & Eliasson 2020). The answer is in the scaling $\chi \propto EB^{-2}$, because in this case $B \approx 3 \text{ nT}$, while in perpendicular shocks $B \approx 30 \text{ nT}$, which

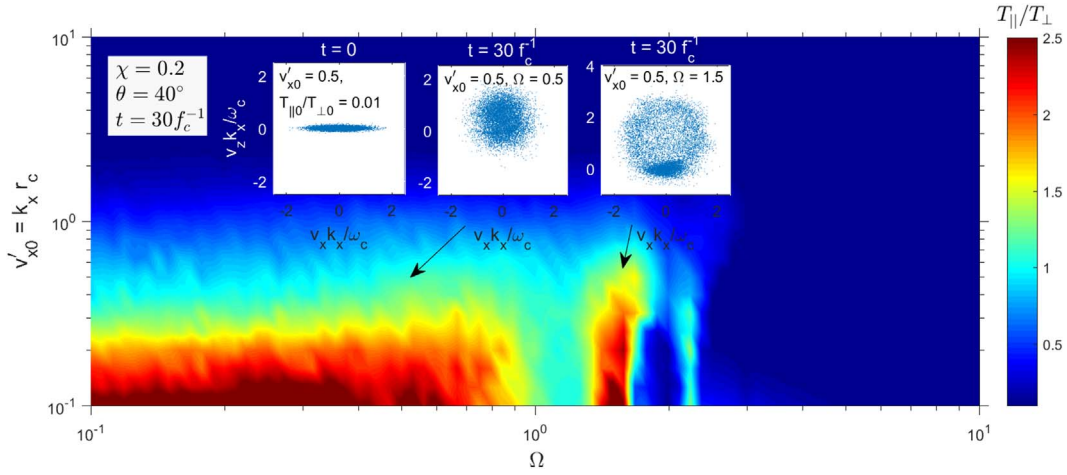


Figure 9. Isotropization of electrons after 30 electron cyclotron periods by waves with normalized amplitude $\chi = 0.2$ and angle $\theta = 40^\circ$ to the magnetic field, and a range of values for Ω and v'_{x0} with the initial temperature anisotropy $\tau = T_{||0}/T_{\perp 0} = 0.01$. The insets show the initial and final distribution functions for $v'_{x0} = 0.5$ and different values of Ω .

gives a factor of 10^{-2} that overrides a factor of 10 in the E -field amplitude.

3.2. Isotropization of the Particle Distribution

In view of the observations in Figures 1(c) that electron distributions are nearly isotropic at shocks, it is of interest to investigate which type of waves are most efficient for the isotropization. We employ a set of test-particle simulation to assess the efficiency of isotropization for obliquely propagating electrostatic waves. Figures 7 and 8 show the time evolutions of the kinetic temperatures as well as the initial and final distribution functions projected in the v_x - v_y and v_x - v_z planes subject to an electrostatic wave propagating respectively at angles $\theta = 40^\circ$ and 60° to the magnetic field, at a normalized frequency $\Omega = 0.5$ and wave amplitude $\chi = 0.2$, for an initial electron distribution function with $v'_{x0} = 0.5$ and an initial temperature anisotropy $\tau = T_{||0}/T_{\perp 0} = 0.01$. For $\theta = 40^\circ$ in Figure 7(a), the electron distribution rapidly becomes isotropic within a few electron cyclotron periods, and the resulting electron distribution function seen in Figure 7(b) becomes almost isothermal in the v_x - v_z plane. In contrast, for $\theta = 60^\circ$ the electrons are only partially isotropized as seen in Figure 8(a), and the resulting distribution at $t = 30 f_c^{-1}$ in Figure 8(b) is nonisothermal in the v_x - v_z plane with a high-velocity tail of electrons in the parallel v_z direction. For both $\theta = 40^\circ$ and 60° the perpendicular velocities are not significantly affected as seen in the v_x - v_y projections of the distribution functions in Figures 7(b) and 8(b). In general, larger values of θ do not lead to isotropization but to resonant acceleration along v_z for lower values of Ω and smaller $v'_{x0} = k_x r_c$.

The efficiency of isotropization for a range of values of Ω and v'_{x0} is shown in Figure 9. Efficient isotropization within a time of 30 cyclotron periods takes place for $\Omega \lesssim 1$ and $v'_{x0} \lesssim 1$, where the resulting electron distribution functions become essentially isotropic. For $1 \lesssim \Omega \lesssim 3$ there are narrow regions where the electrons are resonantly accelerated parallel to the magnetic field lines so that $T_{||} > T_{\perp}$. In this case the electrons have gained a positive mean drift and hence have produced a net current parallel to the magnetic field lines, reflecting the action of a single wave propagating obliquely in the positive direction to the magnetic field. Such currents could be canceled if there are MTS waves propagating at both positive and

negative directions to the magnetic field lines. Isotropization is not efficient for $\Omega > 3$. In short, isotropization takes place for obliquely propagating electrostatic waves with frequencies near or below the electron cyclotron frequency, with wavelengths larger than the electron Larmor radius. We have run isotropization with $\chi = 0.2$ to show that this process occurs for waves with lower amplitudes, and is not necessarily linked with the stochastic heating that requires $\chi > 1$.

4. Conclusions

This research has shown that electrons are heated by two different mechanisms at the Earth's quasi-parallel shock: stochastic and quasi-adiabatic. We have performed detailed analysis of two heating cases identified as “s” stochastic, where the electron temperature was increased by 10 eV, and quasi-adiabatic case “q” with temperature increased by 15 eV. The temperature increase was by a factor of 2 in both cases.

The stochastic heating preferably occurs at low magnetic fields, when the electron heating function $\chi_e = m_e q_e^{-1} B^{-2} \text{div}(\mathbf{E}_{\perp})$ exceeds unity and is accomplished by the perpendicular electric field provided by the ECD instability. We have shown that the bulk heating is most likely done by waves in the frequency range $(0.4-5)f_{ce}$ with wavelengths $\lambda > 2$ km, while the tail of the distribution can be accelerated by shorter waves with higher frequency, $f > 5f_{ce}$. The simulations also indicate that stochastic heating in some cases leads to flat-topped distribution functions frequently observed in the vicinity of shocks in space plasma (Feldman et al. 1983; Lefebvre et al. 2007).

A different heating mechanism takes place in regions where the magnetic field is being compressed, and $|\chi_e| < 1$. In this case the electrons are heated through the conservation of the magnetic moment $\propto T_{e\perp}/B$ in a process identified by Stasiewicz & Eliasson (2020) as quasi-adiabatic. The perpendicular kinetic energy gained is redistributed to the parallel direction by the scattering by waves, leading to an almost isotropic electron distribution, following the isotropic temperature relation $T/B = (T_0/B_0)(B_0/B)^\alpha$ where the value of $\alpha = 1/3-2/3$ depends on the physical processes involved. In the case of quasi-perpendicular shocks (Stasiewicz & Eliasson 2020) the kinetic energy of the electrons is conserved during the isotropization by electrostatic fields, leading to $\alpha = 1/3$. In the present case of quasi-parallel shocks a part of the

perpendicular energy gain is converted to waves causing the isotropization, and it is found that a larger $\alpha = 2/3$ better fits the data.

The observations have been confirmed by test-particle simulations showing rapid heating and isotropization of electrons by electrostatic waves propagating at different angles to the magnetic field. The isotropization is most efficient when electrostatic waves propagate at angles $\lesssim 60^\circ$ to the magnetic field.

The results of this work support the shock heating scenario that starts with compression of the density, which via the initial diamagnetic current triggers consecutively three cross-field current-driven instabilities: LHD \rightarrow MTS \rightarrow ECD, which produce stochastic heating of ions and electrons, in addition to a common quasi-adiabatic heating of electrons on compressions of B .

The authors thank members of the MMS mission for making available the data. MMS science data are made available through the Science Data Center at the Laboratory for Atmospheric and Space Physics (LASP) at the University of Colorado, Boulder: <https://lasp.colorado.edu/mms/sdc/public/>. B.E. acknowledges support from the EPSRC (UK), grants EP/R004773/1 and EP/M009386/1.

Software: Data analysis was performed using the IRFU-Matlab analysis package available at <https://github.com/irfu/irfu-matlab>.

ORCID iDs

Krzysztof Stasiewicz  <https://orcid.org/0000-0002-2872-5279>

Bengt Eliasson  <https://orcid.org/0000-0001-6039-1574>

References

- Balikhin, M., Gedalin, M., & Petrukovich, A. 1993, *PhRvL*, **70**, 1259
 Breneman, A. W., Cattell, C. A., Kersten, K., et al. 2013, *JGR*, **118**, 7654
 Burch, J. L., Moore, R. E., Torbert, R. B., & Giles, B. L. 2016, *SSRv*, **199**, 1
 Daughton, W. 2003, *PhPl*, **10**, 3103

- Davidson, R. C., Gladd, N. T., Wu, C., & Huba, J. D. 1977, *PhFI*, **20**, 301
 Drake, J. F., Huba, J. D., & Gladd, N. T. 1983, *PhFI*, **26**, 2247
 Ergun, R. E., Tucker, S., Westfall, J., et al. 2016, *SSRv*, **199**, 167
 Escoubet, C. P., Schmidt, R., & Russell, C. T. 1997, *SSRv*, **79**, 11
 Feldman, W. C., Anderson, R. C., Bame, S. J., et al. 1983, *JGRA*, **88**, 96
 Forslund, D., Morse, R., Nielson, C., & Fu, J. 1972, *PhFI*, **15**, 1303
 Fukuyama, A., Momota, H., Itatani, R., & Takizuka, T. 1977, *PhRvL*, **38**, 701
 Fuselier, S. A., & Gurnett, D. A. 1984, *JGR*, **89**, 91
 Gary, S. P. 1993, *Theory of Space Plasma Microinstabilities* (Cambridge: Cambridge Univ. Press)
 Gary, S. P., Tokar, R. L., & Winske, D. 1987, *JGRA*, **92**, 10029
 Goodrich, K. A., Ergun, R., Schwartz, S. J., et al. 2018, *JGR*, **123**, 9430
 Harvey, C. C. 1998, in *Analysis Methods for Multi-spacecraft Data*, ed. G. Paschmann & P. W. Daly (Noordwijk: ESA), 307
 Janhunen, S., Smolyakov, A., Sydorenko, D., et al. 2018, *PhPl*, **25**, 082308
 Karney, C. F. F. 1979, *PhFI*, **22**, 2188
 Lashmore-Davies, C., & Martin, T. 1973, *NucFu*, **13**, 193
 Lashmore-Davies, C. N. 1971, *PhFI*, **14**, 1481
 Lefebvre, B., Schwartz, S. J., Fazakerley, A. F., & Decreau, P. 2007, *JGRA*, **112**, A09212
 Lindqvist, P.-A., Olsson, G., Torbert, R. B., et al. 2016, *SSRv*, **199**, 137
 Lucek, E. A., Horbury, T. S., Dandouras, I., & Reme, H. 2008, *JGRA*, **113**, A07S02
 Mallat, S. 1999, *A Wavelet Tour of Signal Processing* (New York: Academic)
 McChesney, J. M., Stern, R., & Bellan, P. M. 1987, *PhRvL*, **59**, 1436
 Mozer, F. S., & Sundqvist, D. 2013, *JGR*, **118**, 5415
 Muschietti, L., & Lembége, B. 2013, *JGR*, **118**, 2267
 Pollock, C., Moore, T., Jacques, A., et al. 2016, *SSRv*, **199**, 331
 Press, W. H., Teukolsky, S. A., Vetterling, W. T., & Flannery, B. P. 2007, *Numerical Recipes: The Art of Scientific Computing* (New York: Cambridge Univ. Press)
 Russell, C. T., Anderson, B. J., Baumjohann, W., et al. 2016, *SSRv*, **199**, 189
 Schwartz, S. J., & Burgess, D. 1991, *GeoRL*, **18**, 373
 Sibeck, D. G., & Angelopoulos, V. 2008, *SSRv*, **141**, 35
 Silveira, O. J. G., Ziebell, L. F., Gaelzer, R., & Yoon, P. H. 2002, *PhRvE*, **65**, 036407
 Stasiewicz, K. 2020a, *MNRAS*, **496**, L133
 Stasiewicz, K. 2020b, *Earth and Space Science Open Archive*, **23**
 Stasiewicz, K., & Eliasson, B. 2020, *ApJ*, **903**, 57
 Stasiewicz, K., Longmore, M., Buchert, S., et al. 2003, *GeoRL*, **30**, 2241
 Torbert, R. B., Russell, C. T., Magnes, W., et al. 2016, *SSRv*, **199**, 105
 Umeda, T., Kidani, Y., Matsukiyo, S., & Yamazaki, R. 2014, *PhPl*, **21**, 022102
 Wilson, L. B., III, Cattell, C. A., Kellogg, P. J., et al. 2010, *JGRA*, **115**, A12104
 Wilson, L. B., III, Koval, A., Sibeck, D., et al. 2013, *JGR*, **118**, 953
 Yoon, P. H., & Lui, A. T. Y. 2004, *JGRA*, **109**, A02210